applied optics

A constrained method for lensless coherent imaging of thin samples

FERRÉOL SOULEZ,[1,*] MANON ROSTYKUS,[2] CHRISTOPHE MOSER,[2] AND MICHAEL UNSER[3]

[1]Univ. Lyon, Univ. Lyon 1, ENS de Lyon, CNRS, Centre de Recherche Astrophysique de Lyon UMR5574, F-69230, Saint-Genis-Laval, France
[2]LAPD, École polytechnique fédérale de Lausanne (EPFL), Lausanne CH-1015, Switzerland
[3]Biomedical Imaging Group, École polytechnique fédérale de Lausanne (EPFL), Lausanne CH-1015, Switzerland
*Corresponding author: ferreol.soulez@univ-lyon1.fr

Received 4 October 2021; revised 15 December 2021; accepted 15 December 2021; posted 16 December 2021 (Doc. ID 445078); published 11 January 2022

Lensless inline holography can produce high-resolution images over a large field of view (FoV). In a previous work [Appl. Opt.60, B38 (2021)], we showed that (i) the actual FoV can be extrapolated outside of the camera FoV and (ii) the effective resolution of the setup can be several times higher than the resolution of the camera. In this paper, we present a reconstruction method to recover high resolution with an extrapolated FoV image of the phase and the amplitude of a sample from aliased intensity measurements taken at a lower resolution.

https://doi.org/10.1364/AO.445078

1. INTRODUCTION

Lensless inline holography is an imaging technique where diffracted light is recorded without any optical parts between the sample and the camera. Given the simplicity, compactness, robustness, and relatively low cost of this setup [1–3], inline digital holography is successfully employed in many applications such as lensfree microscopy [2–5] or metrology [6]. However, unlike direct imaging methods, the recorded hologram cannot be directly visualized. Instead, computational algorithms are required to image the phase and amplitude of the sample or to extract parameters of interest.

The naive backpropagation of the measured hologram to the sample plane leads to the well-known twin-image artifacts caused by the loss of information about phase. Phase retrieval methods rely on either phase diversity and/or prior knowledge of the sample to estimate the missing phase. Phase diversity [7] consists of recording several images with an additional known phase variation (i.e., varying illumination angle [8], wavelength [9–12], or sample-camera distance [9,13–19]). The priors can be enforced by either constraining the solution to belong to a given subspace (e.g., the subspaces of phase- or absorption-only objects or the subspace of objects with a given spatial support [20]) or imposing *a priori* statistics on the object. The most generic way to account for prior knowledge is to introduce a so-called regularization function that favors reconstructions with desirable properties (e.g., smoothness). In diffraction imaging, the most popular priors are the sparsity [16,21–26], total variation [27–30], and learned priors such as dictionary-based [31] or deep-learning plug-and-play [32] regularizations.

The earliest phase-retrieval algorithm is due to Gerchberg and Saxton [13]. It reconstructs a complex wavefront in the object plane from intensity measurements taken at two different depths. This alternating-projection strategy was further improved by Fienup [20,33] and gave birth to a large family of (non-convex) successive projection algorithms [34–38]. The proposed constrained method for lensless coherent imaging (COMCI) originates from these projection methods, as its optimization scheme is the alternating-direction-of-multipliers method (ADMM) [39], where each step makes use of generalized projections (the so-called proximity operator). This ADMM scheme was already successfully used in a phase-retrieval context [40–43].

For a decade, several authors [22–25] have also proposed to address the phase-retrieval problem through convex relaxation. More recently, deep-learning-based methods have also been proposed [44]. A state-of-the-art review of phase-retrieval methods can be found in [29,45].

One of the main advantages of lensless inline holography is that it can produce high-resolution images over a large field of view (FoV), which can be even larger than the camera FoV. Indeed, while most works [40,46–53] restrict the reconstructed FoV to that of the sensor, other works [21,30,54,55] achieve, for similar measurements, the retrieval of information over a much larger FoV.

In a previous work [56], we showed that (i) the actual FoV can be extrapolated outside of the camera FoV and (ii) the resolution is not dependent on sampling by the detector (for instance, in terms of sampling rate, pixel shape, pixel fill factor) and is determined only by the propagation distance z and illumination parameters (wavelength, coherence, incidence angle). From

these parameters, we propose some estimates of the FoV and the resolution of any given setup.

The estimated [56] effective resolution of the setup can be several times higher than that of the camera, even though the recorded signals are often undersampled and the Nyquist criterion not fulfilled. This induces aliasing issues ignored in many works [40,46–50] that reconstruct the object at the same resolution as that of the detector. To overcome this limitation, several methods have proposed to recover aliased spatial frequencies on super-resolved holograms built from subpixel-shifted low-resolution holograms [8,30,51–53,57]. Other works directly reconstruct the object from aliased intensity using prior knowledge on its shape or bandwidth [58–61].

In this paper, we present a reconstruction method that recovers high-resolution, large FoV images of the phase and amplitude of a sample from intensity measurements taken at a lower resolution and over a smaller FoV. It does not need the estimation of superresolution holograms before use. The presented framework is versatile enough to be suitable to a wide range of applications with varying depths, wavelengths, and illuminations. It derives from a similar framework for image reconstruction in optical long-baseline interferometry [42,62] and was already successfully applied in lensless microscopy [2,3].

COMCI has the same objective as the propagation phasor approach proposed in [63], but it has only one stage and no need for superresolution methods while still being able to extrapolate the FoV. Moreover, based on an inverse-problem approach, COMCI is optimal in a likelihood-related statistical sense.

2. IMAGE FORMATION MODEL

A. Notations

We typeset symbols in lowercase for functions and scalars (e.g., o and λ), in boldface lowercase for vectors (e.g., $\boldsymbol{o}$), in uppercase calligraphic for operators acting on functions (e.g., $\mathcal{M}$), and in boldface uppercase for matrices (e.g., $\mathbf{H}$). In this context, *vectors* are collections of values (e.g., dataset, sampled object) while *matrices* are linear mappings that produce vectors when applied to vectors. We denote by $\boldsymbol{x}^\top$ the adjoint (i.e., conjugate transpose) of $\boldsymbol{x}$, $\langle \boldsymbol{x}, \boldsymbol{y}\rangle = \boldsymbol{x}^\top \boldsymbol{y}$ is the scalar product between vectors $\boldsymbol{x}$ and $\boldsymbol{y}$, and $\boldsymbol{x} \times \boldsymbol{y}$ their element-wise (Hadamard) product. The Euclidean norm of $\boldsymbol{x}$ is $||\boldsymbol{x}||_2 = \sqrt{\boldsymbol{x}^\top \boldsymbol{x}}$, while $||\boldsymbol{x}||_{\mathbf{W}} = \sqrt{\boldsymbol{x}^\top \mathbf{W} \boldsymbol{x}}$ is a weighted version of the norm (with $\mathbf{W}$ Hermitian positive semidefinite). With these notations, a wave, say $w \in \mathbb{W}$, is a complex-valued function of the 2D lateral coordinates $\boldsymbol{x} = (x_1, x_2)$. Due to the finite amount of power transported by a physically realistic wave, w is square-integrable; hence, $\mathbb{W}$ is the Hilbert space of square-integrable functions from $\mathbb{R}^2$ to $\mathbb{C}$. The discretized version of this wave is the vector $\boldsymbol{w} = (w_1, \dots, w_N) \in \mathbb{C}^N$ ordered in lexicographical order of N samples. Functions and vectors with a hat (i.e., $\hat{w}$) and without a hat (i.e., w) are in the Fourier and space domains, respectively. We note by $\boldsymbol{\omega} = (\omega_1, \omega_2) \in \mathbb{R}^2$ the 2D angular frequency and by $\mathcal{F}$ the continuous (non-unitary) 2D Fourier-transform operator defined as

$$\hat{f}(\boldsymbol{\omega}) \triangleq \mathcal{F}\{f\}(\boldsymbol{\omega}) = \iint_{\mathbb{R}^2} f(\boldsymbol{x}) \mathrm{e}^{-j\boldsymbol{x}^\top \omega} \mathrm{d}\boldsymbol{x}. \tag{1}$$

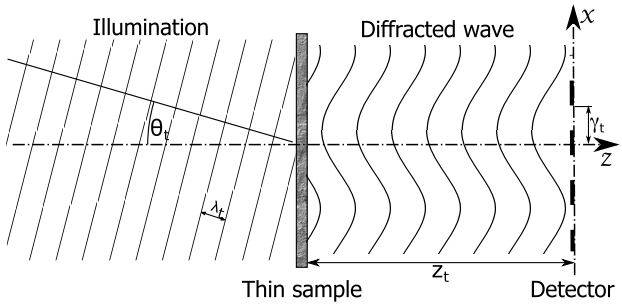

Fig. 1. Setup.

B. Setup

We consider the lensless setup depicted in Fig. 1. There, a thin (2D) sample, described by the function $o : \mathbb{R}^2 \to \mathbb{C}$, is placed orthogonally to the optical axis at $z = 0$. For each observation $t = \{1, \dots, T\}$, the sample is illuminated by the wave u_t of wavelength λ_t (or a wavenumber $k_t = n\frac{2\pi}{\lambda_t}$) arriving at the incidence angle $\boldsymbol{\theta}_t = (\theta_{1,t}, \theta_{2,t})$ relative to the optical axis. After propagation in a medium of refractive index n, the diffracted wave w_t is recorded by a detector of size $(\ell_1 \times \ell_2)$ placed at a distance z_t orthogonally to the optical axis. The detector produces the discrete measurements $\boldsymbol{d}_t \in \mathbb{R}^P$. The detector is of size $\ell = (\ell_1 \times \ell_2)$ with a square pixel pitch of Δ and number of pixels $P = \ell_1 \ell_2 / \Delta^2$.

C. Varying Parameters

The phase-retrieval problem can be solved only by varying the parameters between observations to provide sufficient diversity. The parameters that can vary are:

- the **distance** z_t between the sample and the detector;
- the **wavelength** λ_t or the wavenumber $k_t = n_0 \frac{2\pi}{\lambda_t}$ of the illumination light;
- the illumination wave u_t and its **angle** $\boldsymbol{\theta}_t = (\theta_{1,t}, \theta_{2,t})$ with the optical axis (in addition to providing diversity to solve the phase retrieval, an inclined illumination also increases the spatial resolution through aperture synthesis);
- the lateral **shift** $\boldsymbol{\gamma}_t = (\gamma_{x,1}, \gamma_{y,2})$ of the detector. As no phase diversity is introduced, detector shifts do not add information for phase retrieval.

3. CONTINUOUS MODEL

To interpret the measurements $\boldsymbol{d}_t$, one has to derive a rigorous model that accounts for the totality of the measured information. This model is summarized in the forward operator $\mathcal{H}_t : L^2(\mathbb{R}^2) \to \mathbb{R}^P$ that acts on the Hilbert space of square-integrable functions L^2 and links the object o to the measurements $\boldsymbol{d} \in \mathbb{R}^P$ as in

$$\boldsymbol{d}_t = \mathcal{H}_t(o) + \boldsymbol{e}_t, \tag{2}$$

where $\boldsymbol{e}_t$ is an error term.

A. Sample Illumination

The complex electrical field v_t right after a sample illuminated by a wave u_t with an incident angle $\boldsymbol{\theta}_t$ is

$$v_t(\boldsymbol{x}) = o(\boldsymbol{x}) u_t(\boldsymbol{x}) \exp(j k_t \boldsymbol{x}^\top \sin(\boldsymbol{\theta}_t)). \tag{3}$$

The fact that the incidence is tilted induces a modulation that can be expressed as a $k_t \sin(\boldsymbol{\theta}_t)$ shift in the Fourier domain, defining $\sin(\boldsymbol{\theta}_t) = (\sin(\theta_{1,t}), \sin(\theta_{2,t}))$.

B. Propagation

As lensless setups can have high numerical apertures, the propagation from the sample plane to the detector plane is modeled by the mean of the angular-spectrum (AS) propagation model [47]. Under a tilted illumination; this propagation kernel writes as [56]

$$\hat{h}_t^{\mathrm{AS}}(\boldsymbol{\omega}) = \begin{cases} e^{j z_t \sqrt{k_t^2 - \|\boldsymbol{\omega} + k_t \sin(\boldsymbol{\theta}_t)\|^2}}, & \|\boldsymbol{\omega} + k_t \sin(\boldsymbol{\theta}_t)\|^2 \le k_t^2 \\ 0, & \text{otherwise.} \end{cases} \tag{4}$$

C. Detector Shift

From one measurement to another, the detector may experience lateral shifts $\boldsymbol{\gamma}_t$ with respect to the system of coordinates used in the propagation model. Thus, in the detector plane, the relation between the electrical field in the system of coordinates q_t of the sample and the electrical field in the system of coordinates w_t of the detector is modeled as

$$q_t(\boldsymbol{x} + \boldsymbol{\gamma}_t) = w_t(\boldsymbol{x}). \tag{5}$$

Equivalently, it can also be expressed as a modulation in the Fourier domain:

$$\hat{w}(\boldsymbol{\omega}) = \hat{q}(\boldsymbol{\omega}) e^{-j \boldsymbol{\gamma}_t{}^\top \boldsymbol{\omega}}. \tag{6}$$

D. Overall Model

Taking into an account illumination, propagation, and detector shifts, the model that links the object and the measurements in the detector plane is

$$w_t(\boldsymbol{x}) = \mathcal{F}^{-1}\left\{\hat{h}_t \times \mathcal{F}\{u_t \times o\}\right\}(\boldsymbol{x}) \mathrm{e}^{j k \boldsymbol{x}^\top \sin(\boldsymbol{\theta}_t)}, \tag{7}$$

with the kernel $\hat{h}_t$ given by

$$\hat{h}_t(\boldsymbol{\omega}) = \begin{cases} \mathrm{e}^{j\left(z_t \sqrt{k_t^2 - \|\boldsymbol{\omega} + k_t \sin(\boldsymbol{\theta}_t)\|^2} - \boldsymbol{\gamma}_t{}^\top \boldsymbol{\omega}\right)}, & \|\boldsymbol{\omega} + k_t \sin(\boldsymbol{\theta}_t)\|^2 \le k_t^2 \\ 0, & \text{otherwise} \end{cases}. \tag{8}$$

If the object spatial-frequency bandwidth is narrow or if the paraxial-approximation hypothesis is fulfilled (see [56]), this propagation model can be approximated by

$$\hat{h}_t^{\mathrm{F}}(\boldsymbol{\omega}) = \mathrm{e}^{j\left(k_t z_t - \boldsymbol{\gamma}_t{}^\top \boldsymbol{\omega} - \frac{z_t}{2k_t}\|\boldsymbol{\omega} + k_t \sin(\boldsymbol{\theta}_t)\|^2\right)}. \tag{9}$$

E. Sensing

The intensity of the diffracted wave w_t is sampled on P pixels by the detector according to

$$d_{p,t} = \iint \varphi_{p,t}(\boldsymbol{x}) |w_t(\boldsymbol{x})|^2 \mathrm{d}\boldsymbol{x} + e_{p,t}, \tag{10}$$

where $\varphi_{p,t}(\boldsymbol{x})$ is the response of the pixel p of the observation t at position $\boldsymbol{x}$. The error term $e_{p,t}$ accounts for the noise of the detector, for photon noise, and for approximation errors such as quantization.

4. DISCRETIZATION

A. Field of View and Superresolution

In practice, to numerically model the propagation, one has to establish a discrete version of the equations found in Section 3. To that end, it is important to determine the FoV and the spatial-frequency bandwidth probed by the setup. Due to the bandlimited nature of the propagation kernel given in Eq. (4), the theoretical FoV of a lensless setup is infinite, and its angular spatial-frequency bandwidth is $B = 2k$, centered on $k \sin(\boldsymbol{\theta})$. In a recent paper [56], we derived more realistic bounds on the size $\ell_{t'}$ of the FoV and the bandwidth $B_{t'}$ for the set $\{z_t, \lambda_t, \boldsymbol{\theta}_t, \boldsymbol{\gamma}_t\}$ of setup parameters. These bounds can be easily derived from a few setup properties, namely, the noise level and the spatiotemporal coherence of the source. In this work, we define the FoV and the bandwidth of the object o as the maxima $\ell' = \max_t(\ell'_t)$ and $B' = \max_t(B'_t)$, over all T observations.

To ensure the separability of the likelihood term in the reconstruction algorithm, we impose commensurability between the sampling rates of the detector and object o. Consequently, if we sample the object on a grid, its pixel pitch Δ' is given by an integer superresolution factor S such that

$$\Delta' = \Delta / S, \tag{11}$$

$$S = \left\lceil \frac{\Delta B'}{2\pi} \right\rceil. \tag{12}$$

At optical wavelengths, detectors cannot measure complex amplitudes of the electric field but only the intensity of the light. The Fourier spectrum of the intensity is the auto-correlation of the Fourier spectrum of the complex amplitude [47]. As a consequence, the bandwidth of the intensity can be twice as wide as the bandwidth B' of the diffracted wave w. Thus, in modeling [Eq. (10)] the sensing, w must be oversampled by a factor of two along each dimension before being converted to intensity. Hence for an object $\boldsymbol{o}$ sampled on N pixels, the electric field $\boldsymbol{w}$ in the detector plane must be oversampled on $4N$ pixels.

Among all possible interpolation functions, we choose to sample the functions of the object o, waves w_t, operators, and $\widehat{h_t}$ using Dirac delta functions to form the vectors $\boldsymbol{o} \in \mathbb{C}^N$, $\boldsymbol{u} \in \mathbb{C}^N$, $\boldsymbol{w} \in \mathbb{C}^{4N}$, and $\hat{\boldsymbol{h}}_t \in \mathbb{C}^N$, where

$$o_n = o(\boldsymbol{x}_n), \tag{13}$$

$$u_{t,n} = u(\boldsymbol{x}_{t,n}), \tag{14}$$

$$w_{t,n} = w_t(\boldsymbol{x}_n), \tag{15}$$

$$\hat{h}_{t,n} = \hat{h}_t(\boldsymbol{\omega}_n). \tag{16}$$

Here, $\boldsymbol{x}_n$ is the position of the nth pixel, and $\boldsymbol{\omega}$ is the angular frequency of the nth pixel. It is possible to use better sampling functions when permitted by the spatio-frequency properties of the observed sample [64].

B. Discrete Forward Model

With discretization of Section 4.A, for each observation t, the complex electrical field on the surface of the detector is given by

$$\boldsymbol{w}_t = \mathbf{H}_t \boldsymbol{o}, \tag{17}$$

where the forward operator $\mathbf{H}_t \in \mathbb{C}^{4N\times N}$ is a propagation operator given by

$$\mathbf{H}_t = \mathbf{F}_{4N}^{-1} \cdot \mathbf{Q} \cdot \mathrm{diag}(\hat{\boldsymbol{h}}_t) \cdot \mathbf{F}_N \cdot \mathrm{diag}(\boldsymbol{u}_t), \tag{18}$$

where $\mathbf{F}_N$ is the 2D discrete Fourier operator of size N. $\mathbf{Q} \in \mathbb{C}^{4N\times N}$ is a zero-padding operator accounting for the spatial over-sampling of $\boldsymbol{w}$.

From Eq. (10), this intensity is linked to the measured image intensities $\boldsymbol{d}_t \in \mathbb{R}_+^P$ by

$$d_{p,t} = \sum_{n\in\mathbb{S}_p} \varphi_{p,t,n} \left|w_{n,t}\right|^2 + e_{p,t}. \tag{19}$$

As the wave is sampled at a rate higher than that of the detector, $\mathbb{S}_p$ is the set of samples of the wave $w_{n,t}$ in the sensitive area of the detector pixel p, and $\varphi_{p,t,n} = \varphi_{p,t}(\boldsymbol{x}_n)$ is the discretized response of the pixel p in the observation t for a wave sample at position $\boldsymbol{x}_n$.

5. INVERSE PROBLEM

The goal of this work is to estimate the complex object $\boldsymbol{o}$ from the observation of the diffracted intensity, which is an inverse problem. It is classically solved in a variational framework where one estimates $\boldsymbol{o}^+$ minimizing a cost function built as the sum of the likelihood term $\mathcal{L}$ and a regularization term $\mathcal{R}$ as in

$$\boldsymbol{o}^+ = \mathrm{argmin}_{\boldsymbol{o}\in\mathbb{D}^N}\big(\mathcal{L}(\boldsymbol{o}) + \mu\mathcal{R}(\boldsymbol{o})\big), \tag{20}$$

where $\mathbb{D}$ is the subspace of $\mathbb{C}$ where lies the object. In this approach, known as penalized *maximum likelihood* or *maximum*a posteriori (MAP), the data term is defined according to the forward model and the statistics of the noise, whereas the regularization function is designed to enforce some prior knowledge about the object such as support, nonnegativity, or smoothness.

A. Likelihood

The likelihood term $\mathcal{L}$ is computed according to the forward model described in Section 4.B and the statistics of the noise. We assume that the noise e_p is independent and there is no cross talk between pixels ($\mathbb{S}_p \cap \mathbb{S}_{p'} = \varnothing \forall\ p \neq p'$). As a consequence, the likelihood term is separable with

$$\mathcal{L}(\boldsymbol{o}) = \sum_{t=1}^{T} \sum_{p\in\mathbb{P}_t} \mathcal{L}_{p,t}\left(\sum_{n\in\mathbb{S}_p} \phi_{p,n}\left|w_{n,t}\right|^2\right). \tag{21}$$

The set $\mathbb{P}_t$ provides an easy way to cope with badly measured pixels, such as saturated ones that do not belong to $\mathbb{P}_t$.

In most applications, only two types of noise are considered: non-stationary Gaussian noise or Poisson noise in the low-flux case. In the Gaussian case, the likelihood term writes as

$$\mathcal{L}_{p,t}(x) = \frac{1}{\sigma_{p,t}^2}(x - d_{p,t})^2, \tag{22}$$

where $\sigma_{p,t}^2$ is the variance of the noise at the pixel p of the tth image.

In the photon-counting case, the noise follows a Poisson distribution, and the likelihood function writes as

$$\mathcal{L}_{p,t}(x) = x - d_{p,t}\log(x + \beta_{p,t}), \tag{23}$$

where $\beta_{p,t}$ is the expectation of some spurious independent Poisson process that accounts for incoherent background emission and detector dark current at the pixel p of the tth image.

B. Regularization

The regularization function $\mathcal{R}$ enforces some prior knowledge about the observed sample. In this work, we use total variation [27]. For a complex object $\boldsymbol{o}$, it is

$$\mathcal{R}(\boldsymbol{o}) = \|\mathbf{B}\boldsymbol{o}\|_{2,1} \tag{24}$$

$$= \sum_{n=1}^{N} \|[\mathbf{B}\boldsymbol{o}]_n\|_2, \tag{25}$$

while $\mathbf{B}$ is the spatial gradient operator

$$\mathbf{B} = \begin{bmatrix} \nabla_1 \\ \nabla_2 \end{bmatrix}, \tag{26}$$

where ∇_1 and ∇_2 are finite-difference operators along the horizontal and vertical directions, respectively. Under a circulant boundaries condition, these finite-difference operators can be defined in the Fourier domain as

$$\mathbf{B} = \begin{bmatrix} \mathbf{F}^{-1} \cdot \mathrm{diag}\left(\hat{\boldsymbol{b}}_1\right) \\ \mathbf{F}^{-1} \cdot \mathrm{diag}\left(\hat{\boldsymbol{b}}_2\right) \end{bmatrix} \mathbf{F}, \tag{27}$$

where $\hat{\boldsymbol{b}}_1$ and $\hat{\boldsymbol{b}}_2$ are spatial differentiation operators expressed in the Fourier domain along dimensions 1 and 2, respectively. Compared to the total variation applied separately on the phase and modulus of $\boldsymbol{o}$, as in [65], this complex regularization function enforces a correlation between edges in both real and imaginary parts. This means that different areas of the sample are supposed to differ in their real and imaginary parts or, equivalently, for both the modulus and phase. That makes sense, as different media may differ at the same time in their refractive indices and absorptions.

C. Constraints

Depending on the object, various constraints can be chosen to define the subspace $\mathbb{D}$. We define the characteristic function of the subspace $\mathbb{D}$ as

$$\mathcal{C}_{\mathbb{D}}(x) = \begin{cases} 0, & x \in \mathbb{D} \\ +\infty, & \text{otherwise.} \end{cases} \tag{28}$$

No amplification. As no emission occurs within the sample, the modulus of the object must be lower than one, so that

$$\mathbb{D}_1 = \{x \in \mathbb{C};\ |x| \leq 1\}. \tag{29}$$

Phase-only object. Biological samples are often transparent and can be modeled as phase-only objects. In this case, the modulus of the object is constrained to have a unit modulus leading to

$$\mathbb{D}_2 = \{x \in \mathbb{C};\ |x| = 1\}. \tag{30}$$

Absorption-only object. If the sample is composed of opaque structures, then its phase is null, and its magnitude must be either zero or one. Such a prior is highly non-convex; we relax it to the convex constraint

$$\mathbb{D}_3 = \{x \in \mathbb{R};\ 0 \leq x\ \leq 1\}. \tag{31}$$

Support constraint. The constraint can also be a support constraint, as classically done in phase retrieval [33]. It constrains the object to be one outside of the support $\mathbb{G}$ of the object:

$$\mathbb{D}_4 = \{x_n \in \mathbb{C};\ x_n = 1 \text{ if } n \notin \mathbb{G}\}. \tag{32}$$

6. MINIMIZATION SCHEME

From the forward model of Section 4.B and the separable likelihood in Eq. (21), Eq. (20) can be rewritten in the constrained form, introducing auxiliary variables $\boldsymbol{y} \in \mathbb{C}^N$ and $\boldsymbol{z} \in \mathbb{C}^{2N}$:

$$\begin{aligned} \boldsymbol{o}^+ = \operatorname{argmin}_{\boldsymbol{o}} & \sum_{t=1}^{T}\sum_{p=1}^{P} \mathcal{L}_{p,t}\left(\sum_{m\in\mathbb{S}_p} \phi_{p,n}|w_{m,t}|^2\right) \\ & + \mu\|\boldsymbol{z}\|_{2,1} + \sum_{n}^{N} \mathcal{C}_{\mathbb{D}}(y_n) \\ \text{subject to } & \begin{cases} \mathbf{H}_t\boldsymbol{o} = \boldsymbol{w}_t, & \forall t \\ \boldsymbol{o} = \boldsymbol{y} \\ \boldsymbol{z} = \mathbf{B}\boldsymbol{o} \end{cases}. \end{aligned} \tag{33}$$

These constraints are enforced by means of an augmented-Lagrangian formulation. The augmented Lagrangian is

$$\begin{aligned} & \mathcal{J}(\boldsymbol{o}, \boldsymbol{w}, \boldsymbol{y}, \boldsymbol{z}, \boldsymbol{q}, \boldsymbol{v}, \boldsymbol{r}) \\ & = \sum_{t=1}^{T}\sum_{p=1}^{P} \mathcal{L}_{p,t}\left(\sum_{m\in\mathbb{S}_p} |w_{m,t}|^2\right) \\ & + \mu\sum_{n}^{N} \|\boldsymbol{z}_n\|_{2,1} + \sum_{n}^{N} \mathcal{C}_n(|y_n|^2) \\ & + \frac{\rho_1}{2}\sum_{t=1}^{T} \left\|\mathbf{H}_t\boldsymbol{o} - \boldsymbol{w}_t + \boldsymbol{q}_t\right\|_2^2 \\ & + \frac{\rho_2}{2}\|\boldsymbol{o} - \boldsymbol{y} + \boldsymbol{v}\|_2^2 + \frac{\rho_3}{2}\|\mathbf{B}\boldsymbol{o} - \boldsymbol{z} + \boldsymbol{r}\|_2^2, \end{aligned} \tag{34}$$

where $\boldsymbol{q}_t \in \mathbb{C}^N$, $\boldsymbol{v} \in \mathbb{C}^N$, $\boldsymbol{r} \in \mathbb{C}^{2N}$ are the scaled Lagrange multipliers and $\rho_1 > 0$, $\rho_2 > 0$, and $\rho_3 > 0$ the augmented-penalty scalar parameters. As there are no theoretical guidelines to set this augmented penalty, we choose to rely on the empirical rules described in Section 6.E.

Under this form, the problem can be solved by means of ADMM [39], solving at each iteration k the series of problems

$$\boldsymbol{w}_t^{(k+1)} = \operatorname{prox}_{1/\rho_1\mathcal{L}}\left(\mathbf{H}_t\boldsymbol{o}^{(k)} + \boldsymbol{q}_t^{(k)}\right), \tag{35}$$

$$\boldsymbol{y}^{(k+1)} = \operatorname{prox}_{1/\rho_2\mathcal{C}_{\mathbb{D}}}\left(\boldsymbol{o}^{(k)} + \boldsymbol{v}^{(k)}\right), \tag{36}$$

$$\boldsymbol{z}^{(k+1)} = \operatorname{prox}_{\mu/\rho_3\|\,\|_{2,1}}\left(\mathbf{B}\boldsymbol{o}^{(k)} + \boldsymbol{r}^{(k)}\right), \tag{37}$$

$$\begin{aligned} \boldsymbol{o}^{(k+1)} = \operatorname{argmin}_{\boldsymbol{o}\in\mathbb{C}^N} & \frac{\rho_1}{2}\sum_{t=1}^{T} \left\|\mathbf{H}_t\boldsymbol{o} - \boldsymbol{w}_t^{(k)} + \boldsymbol{q}_t^{(k)}\right\|_2^2 \\ & + \frac{\rho_2}{2}\left\|\boldsymbol{o} - \boldsymbol{y}^{(k)} + \boldsymbol{v}^{(k)}\right\|_2^2 + \frac{\rho_3}{2}\left\|\mathbf{B}\boldsymbol{o} - \boldsymbol{z}^{(k)} + \boldsymbol{r}^{(k)}\right\|_2^2. \end{aligned} \tag{38}$$

Here, $\operatorname{prox}_{1/\rho_1\mathcal{L}}$, $\operatorname{prox}_{1/\rho_2\mathcal{C}_{\mathbb{D}}}$, and $\operatorname{prox}_{\mu/\rho_3\|\,\|_{2,1}}$ are proximity operators (Moreau's proximal mapping operators) of the likelihood function, the constraints characteristic function, and the regularization function, respectively.

At each iteration, the scaled Lagrange multipliers are updated using the rule

$$\boldsymbol{q}_t^{(k+1)} = \boldsymbol{q}_t^{(k)} + \mathbf{H}_t\boldsymbol{o}^{(k+1)} - \boldsymbol{w}_t^{(k+1)}, \tag{39}$$

$$\boldsymbol{v}^{(k+1)} = \boldsymbol{v}^{(k)} + \boldsymbol{y}^{(k+1)} - \boldsymbol{o}^{(k+1)}, \tag{40}$$

$$\boldsymbol{r}^{(k+1)} = \boldsymbol{r}^{(k)} + \mathbf{B}\boldsymbol{o}^{(k+1)} - \boldsymbol{z}_t^{(k+1)}. \tag{41}$$

A. Likelihood Sub-Problem

The solution of the first inner problem Eq. (35) is given by the proximity operator of the likelihood function $\mathcal{L}$. As the likelihood function is separable, its solution is given by the proximity operator of the function $\mathcal{L}_{p,t}$ for each observation t and each low resolution pixel p:

$$\text{prox}_{1/\rho\mathcal{L}_{p,t}}(\boldsymbol{y}) = \text{argmin}_{\boldsymbol{x}}\left(\mathcal{L}_{p,t}(\boldsymbol{x}) + \frac{\rho}{2}\|\boldsymbol{x}-\boldsymbol{y}\|_2^2\right). \quad (42)$$

For Gaussian and Poisson likelihoods, and without cross talk between pixels, this proximity operator admits closed-form solutions [66] that are used further in the paper. A generalization of these proximity operators in the presence of cross talk is proposed in [67].

B. Constraints Sub-Problem

The solution of the second inner problem Eq. (36) is given by the proximity operator of the characteristic function of the constraints. All the constraints described in Section 5.C are separable, and the solution is given for each pixel p by

$$\text{prox}_{1/\rho\mathcal{C}}(y_n) = \text{argmin}_x\left(\mathcal{C}_{\mathbb{D}}(x) + \frac{\rho}{2}\|x-y_n\|_2^2\right). \quad (43)$$

For each constraint described in Section 5.C, this proximity operator is a simple projection on the subspace $\mathbb{D}$ and has a closed-form solution.

C. Regularization Sub-Problem

The solution of the third inner problem Eq. (37) is given by the proximity operator of the mixed norm $||\,||_{2,1}$. This proximity operator has the closed-form solution [68]

$$\left[\text{prox}_{1/\rho\|\,\|_{2,1}}(\boldsymbol{y})\right]_{n,d} = y_{n,d}\left(1-\left(\rho\sqrt{y_{n,1}^2+y_{n,2}^2}\right)^{-1}\right)_+, \quad (44)$$

with $(x)_+ = \max(0, x),\ x \in \mathbb{R}$. The pixel index is given by n, and $d \in \{1, 2\}$ is the direction of the derivative.

D. Fourth (Consensus) Sub-Problem

The fourth problem Eq. (38) is a quadratic problem. It has the closed-form solution

$$\boldsymbol{o}^+ = \left[\frac{\rho_1}{2}\sum_{t=1}^{T}\mathbf{H}_t{}^\top\mathbf{H}_t + \frac{\rho_2}{2} + \frac{\rho_3}{2}\mathbf{B}^\top\mathbf{B}\right]^{-1} \times \left[\frac{\rho_1}{2}\sum_{t=1}^{T}\mathbf{H}_t{}^\top(\boldsymbol{w}_t-\boldsymbol{q}_t) + \frac{\rho_2}{2}(\boldsymbol{y}-\boldsymbol{v}) + \frac{\rho_3}{2}\mathbf{B}^\top(\boldsymbol{z}-\boldsymbol{r})\right]. \quad (45)$$

Unfortunately, in the general case, owing to the size of $\mathbf{H}$ and $\mathbf{B}$, the matrix inversion of the first term cannot be performed in practice. However, this problem can be solved approximately by conjugate-gradient steps as is classically done [39]. In this case, the number M of Fourier transforms of size N computed per iteration is

$$M = M_{\text{CG}}(4T+2) + 2T + 3, \quad (46)$$

where M_{CG} is the number of conjugate-gradient steps. In addition, at each iteration, there are $(T \times P)$ estimations of a root of a cubic or quadratic polynomial needed in Eq. (35).

The use of the conjugate gradient makes the computational burden very high and prevents the use of the algorithm for large problems. However, there are some cases where the exact solution of Eq. (45) can be efficiently estimated: when the illumination is a plane wave and when the illumination is uniform.

1. Plane Wave Illumination

When the sample is illuminated by plane waves, the term $\boldsymbol{u}_t$ in Eq. (3) is constant: $u_{t,p} = a_t, \forall p$. In this case, for each observation t, the matrix $\mathbf{H}_t^\top\mathbf{H}_t$ becomes diagonal in the Fourier domain:

$$\mathbf{H}_t^\top\mathbf{H}_t = |a_t|^2\mathbf{F}^{-1}\text{diag}\left(\left|\hat{\boldsymbol{h}}_t\right|^2\right)\mathbf{F}. \quad (47)$$

The solution of Eq. (38) can be written in the Fourier domain as

$$\hat{\boldsymbol{o}}^+ = \left(\rho_1\sum_{t=1}^{T}a_t^2 + \rho_2 + \rho_3\sum_{d\in\{1,2\}}|\hat{\boldsymbol{b}}_d|^2\right)^{-1} \times \left(\rho_1\sum_{t=1}^{T}a_t\hat{\boldsymbol{h}}_t{}^*(\hat{\boldsymbol{w}}_t-\hat{\boldsymbol{q}}_t) + \rho_2\sum_{d\in\{1,2\}}\hat{\boldsymbol{b}}_d{}^*(\hat{\boldsymbol{z}}_d-\hat{\boldsymbol{r}}_d) + \rho_3(\hat{y}-\hat{v})\right). \quad (48)$$

Let us notice that in this case, it is possible to spare Fourier transform computations by performing all ADMM steps [Eqs. (35)–(38)] in the Fourier domain. Equations (37) and (36) are solved in accordance with the following property of the proximal operator [69]:

$$g(\boldsymbol{x}) = f(\mathbf{F}\boldsymbol{x})\ \&\ \mathbf{F}\mathbf{F}^\top = \mathbf{I} \Rightarrow \text{prox}_g(\boldsymbol{x}) = \mathbf{F}^\top\text{prox}_f(\mathbf{F}\boldsymbol{x}). \quad (49)$$

The number of Fourier transforms per iteration is reduced to

$$M = 2T + 6. \quad (50)$$

2. Uniform Illumination and Fresnel Propagation

In the Fresnel regime, the Fresnel propagation operator $\boldsymbol{h}^F$ described in Eq. (9) has a unit modulus. Whatever the phase of the illumination wave, if its magnitude is uniform ($|u_{t,p}| = b_t, \forall p$), the expression $\mathbf{H}_t^\top\mathbf{H}_t$ becomes

$$\mathbf{H}_t^\top\mathbf{H}_t = b_t^2\mathbf{I}. \quad (51)$$

The matrix inversion Eq. (45) can then be computed efficiently in the Fourier domain. The number of Fourier transforms per iteration becomes

$$M = 4T + 5. \quad (52)$$

E. Setting Parameters

In addition to the hyperparameter μ common to all MAP methods, there are three more parameters to be set in this method: augmentation parameters ρ_1, ρ_2, and ρ_3. As the overall problem is not convex, its solution depends on them. The optimum for

these four parameters cannot be found by trial and error with such iterative methods. Fortunately, after investigating the range of possible parameters, we found empirically the rules

$$\rho = 100\mu, \tag{53}$$

$$\rho_1 = \rho/(TI_0), \tag{54}$$

$$\rho_2 = \rho, \tag{55}$$

$$\rho_3 = \rho, \tag{56}$$

where I_0 is the mean intensity per pixel. These rules are used throughout all our results, leaving only the hyperparameter μ to tune.

The superresolution parameter s is usually set according to the rules derived in [56]. We experimentally found that the hyperparameter μ is approximately independent of this superresolution parameter s. Using this observation, one can rapidly estimate the hyperparameter at a small superresolution before performing a full reconstruction at larger superresolution.

7. NUMERICAL RESULTS

The proposed method covers a wider panel of applications that we can deal with. Nevertheless, we present in this section some results on synthetic data covering typical setups. All simulations and reconstructions presented in this paper were done in MATLAB using the GlobalBioIm library [70]. The open-source code used is available in the COMCI repository [71]. To assess its FoV extrapolation and superresolution capabilities, all COMCI reconstruction were performed on an larger, extended FoV, with smaller pixels than prescribed in [56].

The computation time is dominated by the Fourier transform involved in the propagation modeling. Due to the GPU implementation of the FFT algorithm, it is possible to maintain acceptable processing times despite the method being computationally intensive: a handful to tens of minutes on an NVIDIA TITAN X GPU. However, given the superresolution and the extrapolation capabilities of COMCI, the dimensions of the estimated vectors can reach tens of million pixels. It is limited by the amount of memory of GPU cards to less than (10000×10000) pixels, which corresponds to a few mm^2 sampled at $\lambda/2$.

Whether COMCI was already used in its preliminary form on real experiments ([2,3], its performance was never assessed. We assessed it in terms of actual FoV, resolution, and reconstruction signal-to-noise ratio (SNR). This SNR is computed only on the camera FoV to be comparable with the reconstruction SNR of the error reduction (ER) algorithm, when possible. The ER algorithm [13,33] is an alternating projection algorithm. It consists of propagating the wavefront back and forth between object and detector plane, constraining the modulus of the wavefront to be equal to the square root of the measured intensities in the detector plane, and enforcing prior knowledge on the object by means of constraints as defined in Section 5.C.

The half-pitch resolution of the reconstructed target is given by the finest-resolved element of the target. It can be compared to the theoretical half-pitch resolution at the center of the FoV given by [56]

$$R = \frac{\lambda}{2n_0}\left(\frac{\ell/2}{\sqrt{(\ell/2)^2 + z^2}} + \sin(|\theta|)\right)^{-1}, \tag{57}$$

with $\ell = \max(\ell_1, \ell_2)$ the largest width of the detctor and $\theta = \max(\theta_1, \theta_2)$ the higher illumination angle.

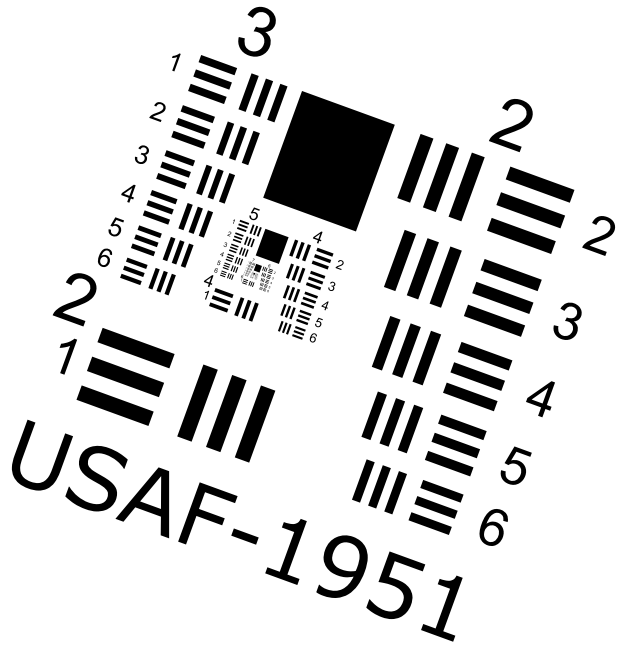

Fig. 2. Vectorial USAF-1951 resolution chart.

A. Simulating Data

To assess the performance of COMCI, we built a synthetic vectorial image of a USAF-1951 resolution target [72] shown in Fig. 2. This vectorial image contains all resolution groups from group -1 to group 11. The smallest resolution element (11-6) has a width of 65 nm.

To avoid the so-called *inverse crime*, where one reconstructs the object from simulated data with exactly the same numerical model as the one used for simulation, the propagation is simulated using bandlimited AS [73] with a very high resolution over a very large FoV that is much larger than the camera FoV. This prevents the border artifacts caused by propagation over a small FoV, as well as the frequency aliasing caused by the undersampling by the camera.

B. Low-Light Single Exposure of Absorbing Object

To assess the performance of COMCI under various noise conditions, we reconstruct an absorbing object from a single exposure for two levels of illumination: a low-light condition with one photon per pixel on average and an intense-light condition with 10^6 photons per pixel. The hologram of an opaque USAF-1951 target is simulated at $z = 1.5$ mm for normal illumination at $\lambda = 532$ nm and a refractive index of one. To prevent aliasing, the propagation is done over (23000×23000) square pixels of width $\Delta_s = 140$ nm.

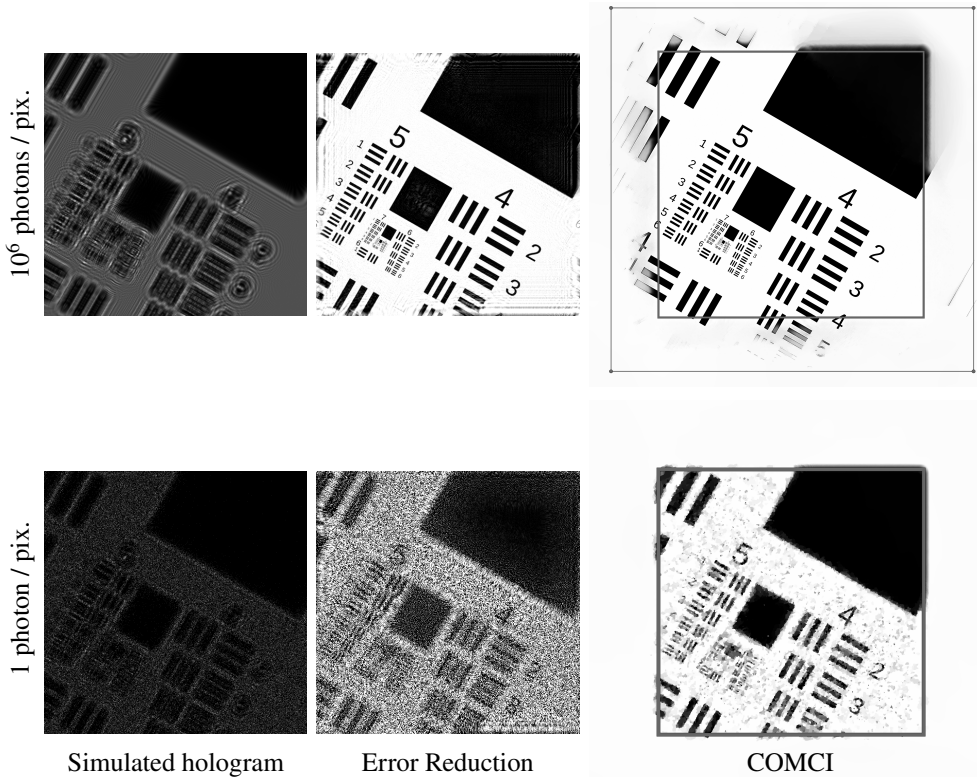

Fig. 3. Simulated hologram and modulus of the reconstructed target by the ER and COMCI algorithms for two levels of flux. On the COMCI reconstruction, the inner square represents the camera FoV, and the outer square represents the extrapolated FoV. As a scalebar, an element of group 5-1 is of size 78×16 μm^2.

Table 1. Reconstruction Parameters and Assessment of Reconstruction Quality for Two Illumination-Flux Cases

	Mean Number of Photons per Pixel	
	1	10^6
Reconstruction Parameters		
Δ' (reconstruction)	560 nm	
FoV	(3120 × 3120) pixels	
	(1.7 × 1.7) mm^2	
μ	0.2	10^{-6}
COMCI		
Extrapolation along each direction	210 μm	14 μm
FoV	(1.57 × 1.57) mm^2	(1.12 × 1.12) mm^2
Half-pitch resolution	7.81 μm	1.1 μm
SNR	14.76 dB	36.25 dB
Error Reduction		
Δ	2.24 μm	
FoV	(1.1 × 1.1) mm^2	(1.1 × 1.1) mm^2
SNR	4.07 dB	19.92 dB
Half-pitch resolution	13.92 μm	2.19 μm

The modeled intensity in the detector plane is then downsampled on pixels of width $\Delta = 2.24$ μm with unit fill factor [$\phi_{p,n} = 1$ in Eq. (21)]. The central area of (512 × 512) pixels is then corrupted by Poisson noise and used as the simulated measurements.

The target is reconstructed in 3000 iterations under an absorption-only object as described in Section 5.C and a likelihood term adapted to photon counting Eq. (23). The data and the reconstructed targets are shown in Fig. 3 and compared to the result of the ER algorithm [74] that appears, in this case, still competitive with the state of the art [75]. Reconstruction parameters and quantitative assessments in terms of size of the FoV, resolution, and reconstruction SNR are given in Table 1. The modulus of the reconstructed target is shown in Fig. 3 with zooms on high-resolution groups in Figs. 4 and 5. Due to the absorption-only constraint, the phase is zero everywhere.

In the high-flux (low-noise) case, the reconstructed target by the ER algorithm is qualitatively good but suffers from border artifacts near the edges of the camera. Its resolution is limited by the sampling of the camera to a half-pitch of 2.19 μm (group 7-6). By comparison, the COMCI reconstruction enjoys a much higher SNR (36.25 dB versus 19.92 dB) and, above all, has high resolution and a larger FoV as predicted from [56]. The extrapolation is clearly visible in Fig. 3. As stated in [56], lensless setups cannot capture low-spatial frequencies from regions outside of the FoV, but the edges of the resolution elements that contain high frequencies are clearly visible as far as 210 μm away from the detector FoV. The smallest element being resolved by the reconstruction is group 8-6, with a half-pitch resolution of 1.1 μm (NA = 0.24), which corresponds to a superresolution factor

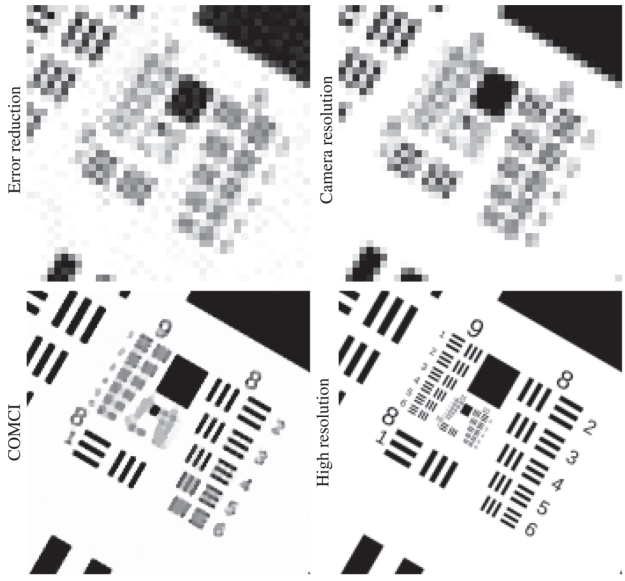

Fig. 5. Zoom on groups 8 and 9 of (a) Fig. 3 in the 10^6 photons/pixel case compared to the ground truth (b) rasterized at the camera resolution (top) and the resolution of the COMCI reconstruction (bottom). As a scalebar, an element of group 6-1 is of size $9.75 \times 1.95\ \mu m^2$.

of $S = 2$ and a space–bandwidth product of thereconstruction almost eight times larger than that of the camera. It is still larger than the theoretical half-pitch resolution at the center of the FoV of $R = 760$ nm.

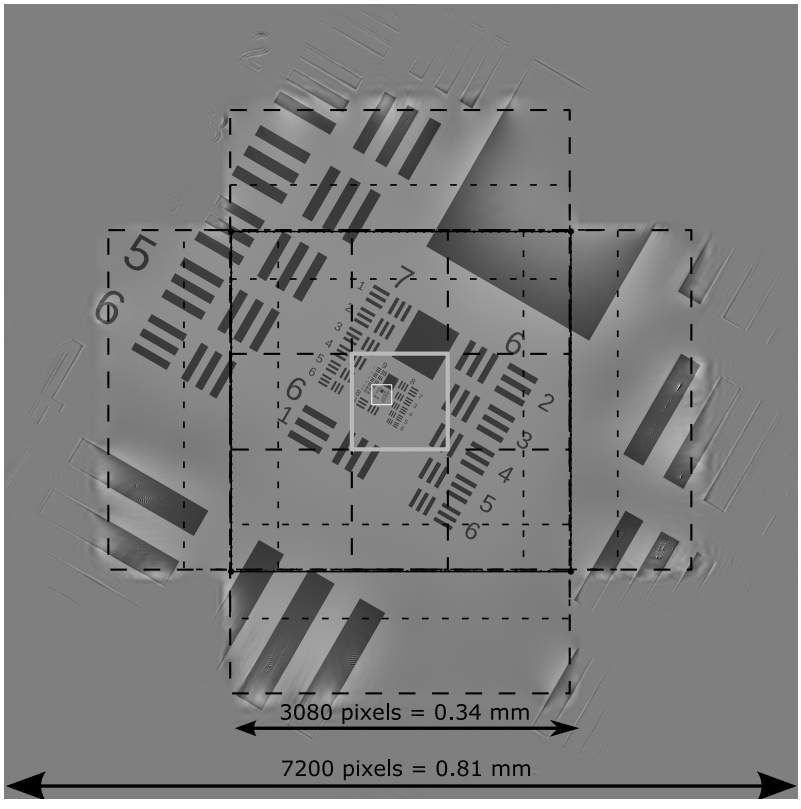

Fig. 6. Reconstructed target in the multiangle case (nine angles). The nine black squares represent the FoV of the nine different measurements. The central gray square depicts the area common to the nine holograms. The very small inner white square covers the zoom on group 10 shown Fig. 7.

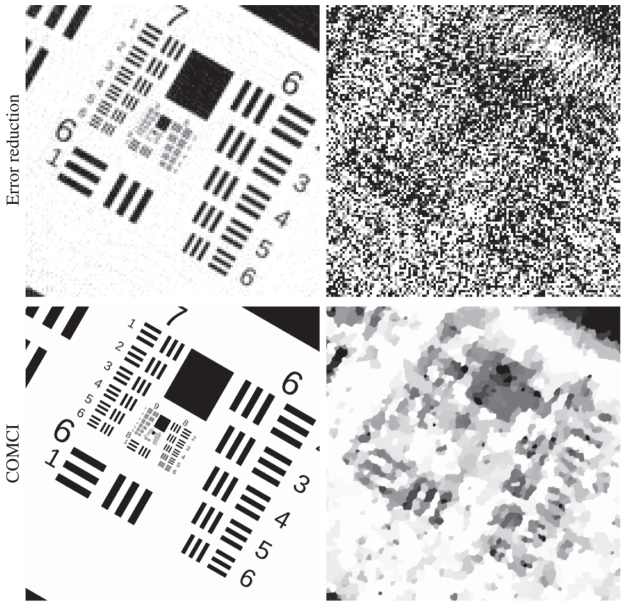

(a) (b)

Fig. 4. Zoom on groups 6 and 7 of the modulus of the reconstructed target by the ER and COMCI algorithms. As a scalebar, an element of group 6-1 is of size 39×7.8 μm^2. (a) 10^6 photons/pix. (b) One photon/pix.

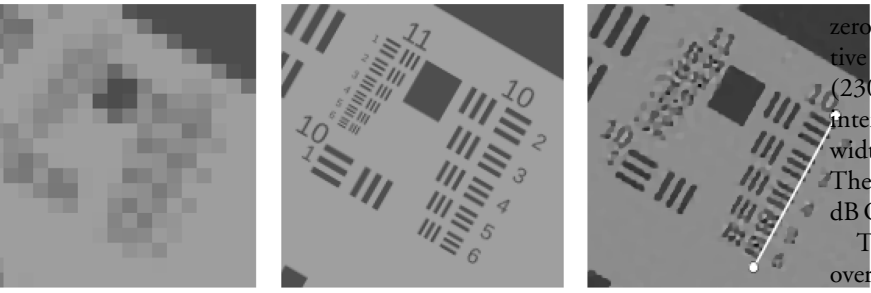

(a) (b) (c)

Fig. 7. Zoom on groups 10 and 11 of the reconstructed target shown as the inner white square in Fig. 6 compared to the ground truth. (a) Target at the camera resolution. (b) Target at reconstruction resolution. (c) Reconstructed phase.

In the very-low-flux case, the ER algorithm fails to reconstruct the target. COMCI achieves the recovery of low-resolution elements down to the 6-1 group. This corresponds to a half-pith of 7.8 μm (NA = 0.03), similar to the theoretical half-pitch resolution at the center of the FoV of 8 μm estimated from [56]. The noise in the measurements almost prevents extrapolation and limits it to a few pixels (14 μm).

C. Multi-Angle Illumination

By combining holograms with various illumination angles, it is possible to increase the resolution by aperture synthesis. We test the performance in resolution of COMCI by simulating nine holograms under various incidence angles, varying $\theta_i \in [-50:25:50]°$ along both axes separately. The simulated target is a transparent USAF-1951 target whose phase is either zero or one. The illumination is at $\lambda = 700$ nm and the refractive index 1.52. The propagation to $z = 0.1$ mm is done over (23000×23000) pixels of width $\Delta_s = 120$ nm. The modeled intensity in the detector plane is then downsampled on pixels of width $\Delta = 1.2$ μm with unit fill factor [$\phi_{p,n} = 1$ in Eq. (21)]. The central area of (308×308) pixels is then corrupted by 60 dB Gaussian noise and used as the simulated measurements.

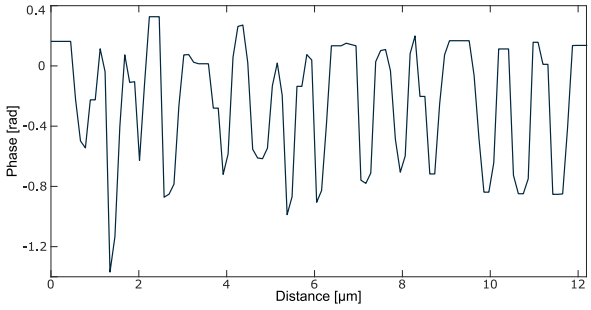

Fig. 8. Profile of the phase of the reconstructed target along the line plotted in Fig. 7(c) along group 10 of the resolution target.

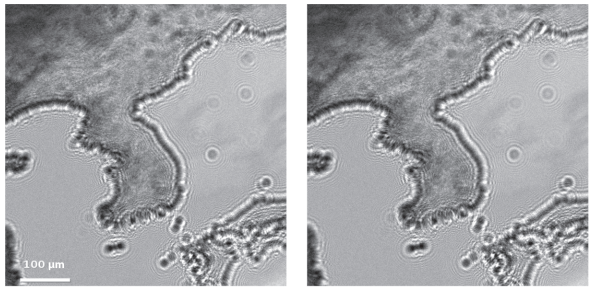

Fig. 9. Simulated data at two different heights.

The target is reconstructed with $\Delta' = 120$ nm pixel pitch over a FoV of (7200×7200) pixels. Its phase, after 3000 iterations, is shown in Fig. 6 with a zoom on group 10 shown in Fig. 7. As a tilted illumination shifts the hologram, the camera FoV varies from one frame to the next. Only a small area of (104×104) μm^2 centered on group 8 is visible on the nine holograms. However, the structures are well recovered even in area in the FoV of only a single hologram. The edges are visible well outside of the FoV of all holograms, which sets the actual reconstructed FoV to (810×810) μm^2, more than five times the detector area. The finest resolved element in Fig. 7 is group 10-6, giving a half-pitch resolution of 275nm (NA = 1.25), at twice the theoretical resolution of $R = 138$ nm. This corresponds to an actual superresolution factor of $S = 4$ and gives a space–bandwidth product of the reconstruction that is 20 times larger than the camera space–bandwidth product. Even at such high resolution, the reconstructed phase is accurate, as can be seen in the profile plotted in Fig. 8 where the phase varies on a range of 1 rad in accordance with the ground truth.

D. Multi-Height Reconstruction

To show the versatility of the COMCI framework, we reconstruct in this section an object with amplitude and phase from measurements with two different distances between the sample

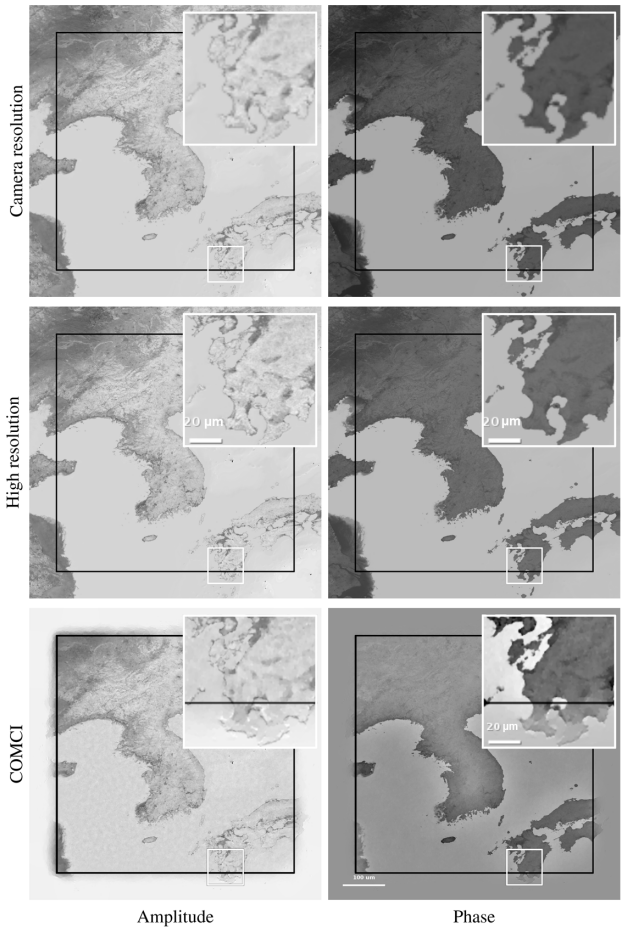

Fig. 10. Amplitude and phase of the reconstructed object from the multi-height data given in Fig. 9. The black square and the white square cover the camera field of view and the area zoomed in the inset, respectively.

and the sensor: $z = \{250, 270\}$ μm. The data were simulated with parameters similar to [63]: a normal incidence illumination at $\lambda = 530$ nm, refractive index of $n_0 = 1$, and camera of (500×500) square pixels of width $\Delta = 1.12$ μm [camera FoV of (560×560) μm^2]. To prevent aliasing, we simulate data over a FoV of (1.3×1.3) mm^2 with pixels of width 93nm. As gigapixel images are needed, we build a ground truth image from a NASA MODIS Earth observation color image, using the hue and saturation channels as the phase and amplitude, respectively. The simulated data are corrupted with 30 dB Gaussian noise and shown in Fig. 9.

According to [56] prescription, the target is reconstructed with $\Delta' = 560$ nm pixel pitch (superresolution $S = 2$) over a FoV of (0.8×0.8) mm^2 $(1432 \times 1432$ pixels). As the object has features in both phase and modulus, it was reconstructed under "no amplification" constraint, enforcing only a modulus equal to or below one. The hyperparameter was set to $\mu = 10^{-2}$. The reconstruction after 3000 iterations is shown in Fig. 10. It shows that on an object much more complex than a USAF-1951 target, the COMCI provides qualitatively good reconstruction in terms of both resolution and FoV extrapolation.

8. CONCLUSION

The key contributions of this paper are twofold. First, we have shown that, as we suggested in [56], it is possible to perform lensless holographic image reconstruction over a FoV larger than the camera FoV with a half-pitch resolution that is several times finer than that of the camera without relying on subpixel-shifted holograms. This means that images are reconstructed with a space–bandwidth product that is an order of magnitude greater than that of the camera (i.e., there are an order of magnitude fewer data than unknowns). Therefore, some prior knowledge must be introduced into the reconstruction process. Second, we have proposed a quantitative reconstruction method (COMCI) that allows us to recover an image over an area five times larger than the camera FoV, with a resolution four times better. COMCI is an open-source generic framework that can be applied to a wide variety of lensless imaging setups (e.g., multi-heights, multi-wavelength, multiangle). It follows a complete "inverse problems" approach that involves three terms: a likelihood term that is adapted to the noise statistics (either Gaussian or Poisson noise); a constraint term that prevents unphysical solutions; and a regularization term that enforces more generic knowledge about the object statistics. The regularization adopted in this work was the general-purpose total variation regularization, which appears to be well suited to the USAF-1951 target. It can easily be replaced by any regularization involving a proximity operator such as learned plug-and-play priors [32]. It is likely that such a regularization will be more effective on biological samples.

Funding. H2020 European Research Council (692726 GlobalBioIm); Région Auvergne-Rhône-Alpes (DIAGHOLO).

Acknowledgment. M.U. was supported by the ERC.

Disclosures. The authors declare no conflicts of interest.

Data Availability. Data underlying the results presented in this paper can be re-simulated thanks to the publicly available code of COMCI in Ref. [71].

REFERENCES

1. O. Mudanyali, D. Tseng, C. Oh, S. O. Isikman, I. Sencan, W. Bishara, C. Oztoprak, S. Seo, B. Khademhosseini, and A. Ozcan, "Compact, light-weight and cost-effective microscope based on lensless incoherent holography for telemedicine applications," Lab Chip **10**, 1417–1428 (2010).
2. M. Rostykus, F. Soulez, M. Unser, and C. Moser, "Compact lensless phase imager," Opt. Express **25**, 4438–4445 (2017).
3. M. Rostykus, F. Soulez, M. Unser, and C. Moser, "Compact in-line lensfree digital holographic microscope," Methods **136**, 17–23 (2018).
4. C. P. Allier, G. Hiernard, V. Poher, and J. M. Dinten, "Bacteria detection with thin wetting film lensless imaging," Biomed. Opt. Express **1**, 762–770 (2010).
5. O. Mudanyali, E. McLeod, W. Luo, A. Greenbaum, A. F. Coskun, Y. Hennequin, C. P. Allier, and A. Ozcan, "Wide-field optical detection of nanoparticles using on-chip microscopy and self-assembled nanolenses," Nat. Photonics **7**, 247–254 (2013).
6. S. Murata and N. Yasuda, "Potential of digital holography in particle measurement," Opt. Laser Technol. **32**, 567–574 (2000).
7. R. A. Gonsalves, "Phase retrieval and diversity in adaptive optics," Opt. Eng. **21**, 215829 (1982).
8. W. Luo, A. Greenbaum, Y. Zhang, and A. Ozcan, "Synthetic aperture-based on-chip microscopy," Light Sci. Appl. **4**, e261 (2015).

9. Y. Zhang, G. Pedrini, W. Osten, and H. J. Tiziani, "Whole optical wave field reconstruction from double or multi in-line holograms by phase retrieval algorithm," Opt. Express **11**, 3234–3241 (2003).
10. P. Bao, F. Zhang, G. Pedrini, and W. Osten, "Phase retrieval using multiple illumination wavelengths," Opt. Lett. **33**, 309–311 (2008).
11. J. Min, B. Yao, M. Zhou, R. Guo, M. Lei, Y. Yang, D. Dan, S. Yan, and T. Peng, "Phase retrieval without unwrapping by single-shot dual-wavelength digital holography," J. Opt. **16**, 125409 (2014).
12. M. Sanz, J. A. Picazo-Bueno, J. Garca, and V. Micó, "Improved quantitative phase imaging in lensless microscopy by single-shot multi-wavelength illumination using a fast convergence algorithm," Opt. Express **23**, 21352–21365 (2015).
13. R. W. Gerchberg and W. O. Saxton, "A practical algorithm for the determination of phase from image and diffraction plane pictures," Optik **35**, 237 (1972).
14. M. R. Teague, "Deterministic phase retrieval: a Green's function solution," J. Opt. Soc. Am. **73**, 1434–1441 (1983).
15. L. Allen and M. Oxley, "Phase retrieval from series of images obtained by defocus variation," Opt. Commun. **199**, 65–75 (2001).
16. Y. Rivenson, Y. Wu, H. Wang, Y. Zhang, A. Feizi, and A. Ozcan, "Sparsity-based multi-height phase recovery in holographic microscopy," Sci. Rep. **6**, 37862 (2016).
17. L. Waller, L. Tian, and G. Barbastathis, "Transport of intensity imaging with higher order derivatives," Opt. Express **18**, 12552–12561 (2010).
18. E. Bostan, E. Froustey, M. Nilchian, D. Sage, and M. Unser, "Variational phase imaging using the transport-of-intensity equation," IEEE Trans. Image Process. **25**, 807–817 (2016).
19. A. Greenbaum and A. Ozcan, "Maskless imaging of dense samples using pixel super-resolution based multi-height lensfree on-chip microscopy," Opt. Express **20**, 3129–3143 (2012).
20. J. R. Fienup, "Phase retrieval algorithms: a comparison," Appl. Opt. **21**, 2758–2769 (1982).
21. L. Denis, D. Lorenz, E. Thiébaut, C. Fournier, and D. Trede, "Inline hologram reconstruction with sparsity constraints," Opt. Lett. **34**, 3475–3477 (2009).
22. Y. Shechtman, A. Beck, and Y. C. Eldar, "Gespar: efficient phase retrieval of sparse signals," IEEE Trans. Signal Process. **62**, 928–938 (2014).
23. E. J. Candès, T. Strohmer, and V. Voroninski, "Phaselift: exact and stable signal recovery from magnitude measurements via convex programming," Commun. Pure Appl. Math. **66**, 1241–1274 (2013).
24. F. Fogel, I. Waldspurger, and A. d'Aspremont, "Phase retrieval for imaging problems," Math. Program. Comput. **8**, 311–335 (2016).
25. T. T. Cai, X. Li, and Z. Ma, "Optimal rates of convergence for noisy sparse phase retrieval via thresholded Wirtinger flow," Ann. Stat. **44**, 2221–2251 (2016).
26. E. J. Candès, X. Li, and M. Soltanolkotabi, "Phase retrieval via Wirtinger flow: theory and algorithms," IEEE Trans. Inf. Theory **61**, 1985–2007 (2015).
27. L. I. Rudin, S. Osher, and E. Fatemi, "Nonlinear total variation based noise removal algorithms," Physica D **60**, 259–268 (1992).
28. H. Chang, Y. Lou, M. K. Ng, and T. Zeng, "Phase retrieval from incomplete magnitude information via total variation regularization," SIAM J. Sci. Comput. **38**, A3672–A3695 (2016).
29. F. Momey, L. Denis, T. Olivier, and C. Fournier, "From Fienup's phase retrieval techniques to regularized inversion for in-line holography: tutorial," J. Opt. Soc. Am. A **36**, D62–D80 (2019).
30. C. Fournier, F. Jolivet, L. Denis, N. Verrier, E. Thiebaut, C. Allier, and T. Fournel, "Pixel super-resolution in digital holography by regularized reconstruction," Appl. Opt. **56**, 69–77 (2016).
31. A. M. Tillmann, Y. C. Eldar, and J. Mairal, "DOLPHIn—dictionary learning for phase retrieval," IEEE Trans. Signal Process. **64**, 6485–6500 (2016).
32. X. Chang, L. Bian, and J. Zhang, "Large-scale phase retrieval," eLight **1**, 4 (2021).
33. J. Fienup, "Iterative method applied to image reconstruction and to computer-generated holograms," Opt. Eng. **19**, 193297 (1980).
34. A. Levi and H. Stark, "Image restoration by the method of generalized projections with application to restoration from magnitude," J. Opt. Soc. Am. A **1**, 932–943 (1984).
35. H. H. Bauschke, P. L. Combettes, and D. R. Luke, "Phase retrieval, error reduction algorithm, and Fienup variants: a view from convex optimization," J. Opt. Soc. Am. A **19**, 1334–1345 (2002).
36. H. H. Bauschke, P. L. Combettes, and D. R. Luke, "Hybrid projection–reflection method for phase retrieval," J. Opt. Soc. Am. A **20**, 1025–1034 (2003).
37. V. Elser, "Solution of the crystallographic phase problem by iterated projections," Acta Crystallogr. A **59**, 201–209 (2003).
38. D. R. Luke, "Relaxed averaged alternating reflections for diffraction imaging," Inverse Prob. **21**, 37 (2005).
39. S. Boyd, N. Parikh, E. Chu, B. Peleato, and J. Eckstein, "Distributed optimization and statistical learning via the alternating direction method of multipliers," Found. Trends Mach. Learn. **3**, 1–122 (2010).
40. A. Migukin, V. Katkovnik, and J. Astola, "Wave field reconstruction from multiple plane intensity-only data: augmented Lagrangian algorithm," J. Opt. Soc. Am. A **28**, 993–1002 (2011).
41. Z. Wen, C. Yang, X. Liu, and S. Marchesini, "Alternating direction methods for classical and ptychographic phase retrieval," Inverse Prob. **28**, 115010 (2012).
42. A. Schutz, A. Ferrari, D. Mary, F. Soulez, É. Thiébaut, and M. Vannier, "Painter: a spatiospectral image reconstruction algorithm for optical interferometry," J. Opt. Soc. Am. A **31**, 2334–2345 (2014).
43. D. Weller, A. Pnueli, G. Divon, O. Radzyner, Y. Eldar, and J. Fessler, "Undersampled phase retrieval with outliers," IEEE Trans. Comput. Imaging **1**, 247–258 (2015).
44. Y. Rivenson, Y. Wu, and A. Ozcan, "Deep learning in holography and coherent imaging," Light Sci. Appl. **8**, 85 (2019).
45. Y. Shechtman, Y. C. Eldar, O. Cohen, H. N. Chapman, J. Miao, and M. Segev, "Phase retrieval with application to optical imaging: a contemporary overview," IEEE Signal Process. Mag. **32**(3), 87–109 (2015).
46. U. Schnars and W. Jüptner, "Direct recording of holograms by a CCD target and numerical reconstruction," Appl. Opt. **33**, 179–181 (1994).
47. J. Goodman, *Introduction to Fourier Optics* (Roberts and Company, 2004).
48. J. H. Milgram and W. Li, "Computational reconstruction of images from holograms," Appl. Opt. **41**, 853–864 (2002).
49. F. Dubois, O. Monnom, C. Yourassowsky, and J.-C. Legros, "Border processing in digital holography by extension of the digital hologram and reduction of the higher spatial frequencies," Appl. Opt. **41**, 2621–2626 (2002).
50. T. Latychevskaia and H.-W. Fink, "Resolution enhancement in digital holography by self-extrapolation of holograms," Opt. Express **21**, 7726–7733 (2013).
51. W. Bishara, T.-W. Su, A. F. Coskun, and A. Ozcan, "Lensfree on-chip microscopy over a wide field-of-view using pixel super-resolution," Opt. Express **18**, 11181–11191 (2010).
52. J. Zhang, J. Sun, Q. Chen, J. Li, and C. Zuo, "Adaptive pixel-super-resolved lensfree in-line digital holography for wide-field on-chip microscopy," Sci. Rep. **7**, 11777 (2017).
53. Z. Luo, A. Yurt, R. Stahl, A. Lambrechts, V. Reumers, D. Braeken, and L. Lagae, "Pixel super-resolution for lens-free holographic microscopy using deep learning neural networks," Opt. Express **27**, 13581–13595 (2019).
54. T. M. Kreis, M. Adams, and W. P. O. Jueptner, "Methods of digital holography: a comparison," in *Optical Inspection and Micromeasurements II*, C. Gorecki, ed. (SPIE, 1997).
55. F. Soulez, L. Denis, É. Thiébaut, C. Fournier, and C. Goepfert, "Inverse problem approach in particle digital holography: out-of-field particle detection made possible," J. Opt. Soc. Am. A **24**, 3708–3716 (2007).
56. F. Soulez, "Gauging diffraction patterns: field of view and bandwidth estimation in lensless holography," Appl. Opt. **60**, B38–B48 (2021).
57. A. Greenbaum, W. Luo, B. Khademhosseinieh, T.-W. Su, A. F. Coskun, and A. Ozcan, "Increased space-bandwidth product in pixel super-resolved lensfree on-chip microscopy," Sci. Rep. **3**, 1717 (2013).
58. L. Onural, "Sampling of the diffraction field," Appl. Opt. **39**, 5929–5935 (2000).
59. A. Stern and B. Javidi, "Improved-resolution digital holography using the generalized sampling theorem for locally band-limited fields," J. Opt. Soc. Am. A **23**, 1227–1235 (2006).

60. F. Soulez, L. Denis, C. Fournier, É. Thiébaut, and C. Goepfert, "Inverse-problem approach for particle digital holography: accurate location based on local optimization," J. Opt. Soc. Am. A **24**, 1164–1171 (2007).
61. C. Fournier, L. Denis, and T. Fournel, "On the single point resolution of on-axis digital holography," J. Opt. Soc. Am. A **27**, 1856–1862 (2010).
62. F. Soulez, É. Thiébaut, J. Kluska, M. Tallon, A. Schutz, and A. Ferrari, "Direct temperature map estimation in optical long baseline interferometry," Proc. SPIE **9907**, 99070Z (2016).
63. W. Luo, Y. Zhang, Z. Göröcs, A. Feizi, and A. Ozcan, "Propagation phasor approach for holographic image reconstruction," Sci. Rep. **6**, 22738 (2016).
64. N. Chacko, M. Liebling, and T. Blu, "Discretization of continuous convolution operators for accurate modeling of wave propagation in digital holography," J. Opt. Soc. Am. A **30**, 2012–2020 (2013).
65. A. Bourquard, N. Pavillon, E. Bostan, C. Depeursinge, and M. Unser, "A practical inverse-problem approach to digital holographic reconstruction," Opt. Express **21**, 3417–3433 (2013).
66. F. Soulez, É. Thiébaut, A. Schutz, A. Ferrari, F. Courbin, and M. Unser, "Proximity operators for phase retrieval," Appl. Opt. **55**, 7412–7421 (2016).
67. B. Roig-Solvas, L. Makowski, and D. H. Brooks, "A proximal operator for multispectral phase retrieval problems," SIAM J. Optim. **29**, 2594–2607 (2019).
68. M. Fornasier and H. Rauhut, "Recovery algorithms for vector-valued data with joint sparsity constraints," SIAM J. Numer. Anal. **46**, 577–613 (2008).
69. P. L. Combettes and J.-C. Pesquet, "A Douglas–Rachford splitting approach to nonsmooth convex variational signal recovery," IEEE J. Sel. Top. Signal Process. **1**, 564–574 (2007).
70. E. Soubies, F. Soulez, M. T. McCann, T.-A. Pham, L. Donati, T. Debarre, D. Sage, and M. Unser, "Pocket guide to solve inverse problems with GlobalBioIm," Inverse Prob. **35**, 104006 (2019).
71. F. Soulez, "COMCI," https://github.com/FerreolS/COMCI.
72. F. Soulez, "USAF 1951," https://figshare.com/articles/figure/USAF_1951/7998134/1.
73. K. Matsushima and T. Shimobaba, "Band-limited angular spectrum method for numerical simulation of free-space propagation in far and near fields," Opt. Express **17**, 19662–19673 (2009).
74. J. R. Fienup, "Reconstruction of an object from the modulus of its Fourier transform," Opt. Lett. **3**, 27–29 (1978).
75. R. Chandra, T. Goldstein, and C. Studer, "Phasepack: A phase retrieval library," in *13th International conference on Sampling Theory and Applications (SampTA)* (IEEE, 2019), pp. 1–5.